

BumpNet: A Sparse Neural Network Framework for Learning PDE Solutions

Shao-Ting Chiu¹ Ioannis G. Kevrekidis² Ulisses Braga-Neto¹

Abstract

We introduce BumpNet, a sparse neural network framework for PDE numerical solution and operator learning. BumpNet is based on meshless basis function expansion, in a similar fashion to radial-basis function (RBF) networks. Unlike RBF networks, the basis functions in BumpNet are constructed from ordinary sigmoid activation functions. This enables the efficient use of modern training techniques optimized for such networks. All parameters of the basis functions, including shape, location, and amplitude, are fully trainable. Model parsimony and h-adaptivity are effectively achieved through dynamically pruning basis functions during training. BumpNet is a general framework that can be combined with existing neural architectures for learning PDE solutions: here, we propose Bump-PINNs (BumpNet with physics-informed neural networks) for solving general PDEs; Bump-EDNN (BumpNet with evolutionary deep neural networks) to solve time-evolution PDEs; and Bump-DeepONet (BumpNet with deep operator networks) for PDE operator learning. Bump-PINNs are trained using the same collocation-based approach used by PINNs, Bump-EDNN uses a BumpNet only in the spatial domain and uses EDNNs to advance the solution in time, while Bump-DeepONets employ a BumpNet regression network as the trunk network of a DeepONet. Extensive numerical experiments demonstrate the efficiency and accuracy of the proposed architecture.

1. Introduction

Physics-Informed Neural Networks (PINNs) (Raissi et al., 2019) and neural operators for PDE-related problems, such

¹Department of Electrical and Computer Engineering, Texas A&M University, TX, USA ²Department of Chemical and Biomolecular Engineering, The Johns Hopkins University, MD, USA. Correspondence to: Shao-Ting Chiu <stchiu@tamu.edu>, Ulisses Braga-Neto <ulisses@tamu.edu>.

In Review

as the Deep Operator Network (DeepONet) (Lu et al., 2021a), have been demonstrated to be effective in learning the solutions of partial differential equations (PDEs), particularly due to their mesh-free nature and their capacity for forward and inverse modeling (Karniadakis et al., 2021). However, they typically rely on deep neural networks with fully-connected layers, leading to high computational demands and limited interpretability of model behavior.

Radial-Basis Function (RBF) neural networks provide an efficient and interpretable alternative that overcomes these limitations (Montazer et al., 2018). RBF neural networks are typically “shallow”, which makes them very efficient in terms of parameter count and training time. They are also interpretable, as the final trained location and shape of the learned basis functions can be observed directly. A limitation of traditional RBF neural network schemes is the use of specialized nonlinearities to implement the basis functions directly. This constrains the shape of the basis functions to be non-trainable and fixed. In addition, it is often the case that the centers of the basis functions are fixed, as well.

To address these limitations, we propose BumpNet, a novel sparse neural network framework for function approximation. BumpNet constructs adaptive localized basis functions (“bumps”) from a linear combination of ordinary sigmoid nonlinearities. The ability of ordinary sigmoid neural networks to produce localized “bumps” was noted already in (Lapedes & Farber). Here, we have developed a *weighting scheme* to construct each bump in such a way that their location, shape, sharpness, and orientation are fully trainable.

We demonstrate that BumpNet can efficiently solve partial differential equations (PDEs) by introducing Bump-PINNs, which use a collocation-type approach similar to PINNs (Raissi et al., 2019). Bump-PINNs have enhanced convergence speed, accuracy, and a significantly reduced parameter count in comparison with ordinary PINNs. Virtually any technique utilized to improve the accuracy of PINNs can be applied to Bump-PINNs as well. Here, we demonstrate the use of self-adaptive weights (McClenny & Braga-Neto, 2023) to improve the performance of Bump-PINNs.

In time-evolution problems, Bump-PINNs can employ

“space-time” bumps. An alternative that can be more efficient and accurate employs a Bump-PINN to approximate the spatial component in connection with a scheme to advance the solution in time, in a manner similar to finite element methods for time-evolution PDEs. Here, we propose Bump-EDNN, which trains a BumpNet neural network to represent the initial condition and uses the evolutionary neural network methodology proposed in (Du & Zaki, 2021) to advance the solution in time.

In addition, we demonstrate that BumpNet can be used in operator learning problems. In parametric PDE applications, the goal is to approximate the operator that maps between the parameter space (which may consist of equation coefficients, source terms, or initial/boundary conditions) and the solution space, in order to obtain a fast surrogate in many-query applications, such as design optimization or uncertainty quantification, when the parameter space must be sampled repetitively. DeepONets (Lu et al., 2021a) are a popular and powerful neural operator architecture. Here, we propose Bump-DeepONet, which employs a BumpNet as the trunk network of a DeepONet. Bump-DeepONets accelerate convergence and reduce the overall parameter count of ordinary DeepONets, making it an efficient option for operator learning tasks.

Finally, model order reduction can be achieved easily in the BumpNet framework through adaptive pruning. We introduce an amplitude-based pruning method, which systematically removes low-amplitude bumps during training, thereby achieving h-adaptivity and enhancing training convergence.

1.1. Related Work

Radial basis function (RBF) methods have a long history in computational science as meshless alternatives to traditional PDE solvers (Belytschko et al., 1996; Bollig et al., 2012; Wang; Montazer et al., 2018). PDE solving with RBF methods is typically based on a collocation approach, where the PDE residue of the basis-function approximation is minimized on a chosen set of points (Zhang et al.; Kansa, a;b). Radial Basis Function (RBF) neural networks were introduced in (Broomhead) as a framework for multi-variable functional interpolation by interpreting learning in neural networks as an interpolation task.

Neural networks are interpreted as adaptive basis functions expansions in (Cyr et al.), leading to a new training strategy that alternates between least squares and gradient descent (LSGD). In a similar vein, the “Extreme Learning Machine” (ELM) (Huang et al., 2006) employs two-layer feedforward neural networks (SLFNs) that avoid iterative tuning by randomly assigning hidden node weights and analytically solving for output weights using a least-squares approach. Physics-informed radial basis neural networks

have been shown to outperform conventional PINNs on problems with fine-scale features and irregular domains (Bai et al., 2023).

The most related methodology to the proposed BumpNet framework is SPINN(Ramabathiran & Ramachandran), which is a sparse, interpretable neural network architecture for solving PDEs. Rather than purely using sigmoids to build the basis functions, SPINN still computes explicitly the distance between input and each bump centers, followed by neural-network approximations to the kernel function. SPINN is not designed for operator learning. We compare Bump-PINNs and Bump-EDNN to SPINN in the experimental section. The result shows that BumpNet achieves improved speed and accuracy.

Another closely related work is the hierarchical deep-learning neural network finite element method (HiDeNN-FEM) (Zhang et al., 2021). Developed independently from BumpNet, HiDeNN-FEM does construct the basis function using just neural network nonlinearities, but it is restricted to the piecewise-polynomial basis functions commonly encountered in FEM implementations, while the basis functions in BumpNet can be constructed from arbitrary sigmoids and are oriented arbitrarily in space. Another difference is that BumpNet uses basis function pruning to achieve h-adaptivity, while HiDeNN-FEM achieves this by adding new basis functions.

1.2. Main Contributions

BumpNet is a novel sparse, interpretable two-layer neural network architecture that implements a basis function expansion. The primary contributions introduced by BumpNet are as follows:

- 1. Flexible Framework for Learning PDE Solutions:** BumpNet leverages a sigmoidal neural network-based approach to construct basis functions, which can be adapted to solve both physics-informed machine learning and operator learning problems.
- 2. Pruning for h-Adaptivity:** We propose a simple pruning strategy during training that allows the basis functions to concentrate in areas of high gradient. This improves model accuracy while reducing model size.
- 3. Sparsity for Efficient Training:** The inherent sparsity of BumpNet enables efficient training with a small number of parameters and faster inference times.

2. Methods

The core of the BumpNet framework is a modular architecture that constructs basis functions (“bumps”) with regular sigmoidal neurons plus a *weight-tying scheme*. BumpNets

are interpretable, in the sense that there are simple formulas relating the shape, location, and amplitude of each bump in terms of the neural network weights.

2.1. BumpNet Architecture

To facilitate understanding, we begin by considering the two-dimensional case, and generalize to the n -dimensional case in the next section. We consider the tanh sigmoid throughout (using other sigmoids requires minor changes to the architecture). The output of a BumpNet for regression in the two-dimensional case is given by

$$\psi(x_1, x_2) = \sum_{i=1}^m h^i \psi^i(x_1, x_2), \quad (1)$$

where m is a hyperparameter indicating the (initial) number of basis functions in the expansion, the h^i are trainable bump height parameters, for $i = 1, \dots, m$, and the i th basis function is given by

$$\begin{aligned} \psi^i(x_1, x_2) = & \frac{1}{2} \tanh(p^i (\tanh(p^i (x_1 + a^i x_2 + s_1^i))) \\ & + \tanh(p^i (-a^i x_1 + x_2 + s_2^i))) \\ & + \tanh(p^i (-x_1 - a^i x_2 + \bar{s}_1^i)) \\ & + \tanh(p^i (a^i x_1 - x_2 + \bar{s}_2^i)) - 3)) + 1, \end{aligned} \quad (2)$$

corresponding to the architecture displayed in Fig. 1. The weights of this neural network are the (1) biases $s_1^i, s_2^i, \bar{s}_1^i, \bar{s}_2^i \in \mathbb{R}$, (2) rotation coefficient $a^i \in \mathbb{R}$, and (3) sharpness factor $p^i \in \mathbb{R}^+$, for $i = 1, \dots, m$. Note that some weights are nontrainable (e.g., the 1 and -1 weights), and some weights are tied, i.e., they are mutually constrained (e.g. the a^i and $-a^i$ weights must be the negative of each other, while the ‘‘sharpness factor’’ p^i is the same for all neurons). This architecture and weight-tying scheme guarantee that $\psi^i(x_1, x_2)$ has the shape of a two-dimensional ‘‘bump’’ over the domain. See Fig. 2 for a visualization for a specific setting of the weights.

The four neurons in the first layer in Fig. 1 define a rectangular support for the bump that is the intersection of the four half-planes defined by

$$\begin{aligned} H_1^i : & x_1 + a^i x_2 + s_1^i \geq 0, \\ H_2^i : & -a^i x_1 + x_2 + s_2^i \geq 0, \\ \bar{H}_1^i : & -x_1 - a^i x_2 + \bar{s}_1^i \geq 0, \\ \bar{H}_2^i : & a^i x_1 - x_2 + \bar{s}_2^i \geq 0. \end{aligned} \quad (3)$$

Note that the boundaries of H_1 and \bar{H}_1 are parallel to each other, and similarly for H_2 and \bar{H}_2 . It is easy to see that the

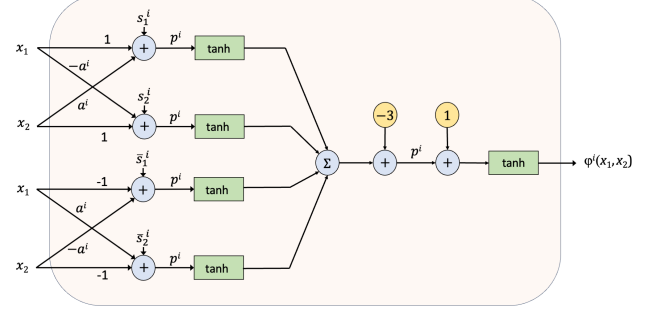


Figure 1: Network architecture of a 2D BumpNet basis module, assuming the tanh sigmoid. The output over the domain is a 2D bump, as seen in Fig. 2.

the rectangular support sides are given by

$$\begin{aligned} l_1^i &= \frac{s_1^i + \bar{s}_1^i}{\sqrt{(a^i)^2 + 1}}, \\ l_2^i &= \frac{s_2^i + \bar{s}_2^i}{\sqrt{(a^i)^2 + 1}}, \end{aligned} \quad (4)$$

while the bump center coordinates are

$$\begin{aligned} c_1^i &= \frac{(\bar{s}_1^i - s_1^i) - a^i(\bar{s}_2^i - s_2^i)}{2((a^i)^2 + 1)}, \\ c_2^i &= \frac{a_i(s_1^i - \bar{s}_1^i) + (\bar{s}_2^i - s_2^i)}{2((a^i)^2 + 1)}. \end{aligned} \quad (5)$$

The interpretability of BumpNet comes from the fact that the support sizes, centers, orientation, sharpness, and height of each bump can be read from the trained BumpNet directly, as seen above.

2.2. Generalization to n Dimensions

In n dimensions, the output of a BumpNet for regression is

$$\psi(\mathbf{x}) = \sum_{i=1}^m h^i \psi^i(\mathbf{x}), \quad (6)$$

for $\mathbf{x} \in \mathbb{R}^n$, where m is the number of basis functions and

$$\begin{aligned} \psi^i(\mathbf{x}) = & \text{squash} \left(\sum_{j=1}^n \tanh(p^i(\mathbf{x}^T \beta_j^i + s_j^i)) \right. \\ & \left. + \sum_{j=1}^n \tanh(p^i(-\mathbf{x}^T \beta_j^i + \bar{s}_j^i)) - (2n-1) \right). \end{aligned} \quad (7)$$

where

$$\text{squash}(x) = \frac{1}{2}(1 + \tanh(p_i x)). \quad (8)$$

Hence, there are now $2n$ neurons in the first layer of each BumpNet module, with weights (β_j^i, s_j^i) and $(-\beta_j^i, \bar{s}_j^i)$,

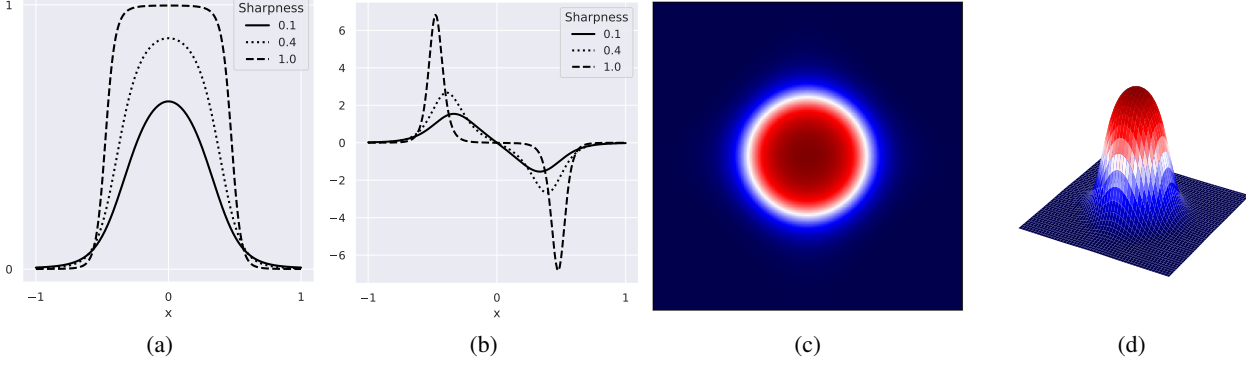


Figure 2: Line profile of a 2D bump in (a) and its derivative (b) for varying sharpness factor value. The bump is located at the origin with unit sides. The bumps plotted in (c) and (d) have a sharpness factor of 0.1.

$j = 1, \dots, n$. In order to determine the weight-tying scheme for the direction vectors β_j^i , note that we need n orthogonal pairs of half-spaces to define the support of the i th bump. The j th pair of half-spaces is:

$$\begin{aligned} H_j^i : \mathbf{x}^T \beta_j^i + s_j^i &\geq 0, \\ \bar{H}_j^i : -\mathbf{x}^T \beta_j^i + \bar{s}_j^i &\geq 0, \end{aligned} \quad (9)$$

We can make the first pair of half-spaces be oriented in an arbitrary direction by letting $\beta_1^i = [1, a_1^i, \dots, a_{n-1}^i]^T$, where a_1^i, \dots, a_{n-1}^i are arbitrary real numbers. The remaining half-space pairs can be determined by using the constraint that they must be orthogonal to the first pair and orthogonal to each other. One way to do this is to find values of β_j^i using the Gram-Schmidt orthogonalization process on the full-rank $n \times n$ matrix $[\beta_1^i, e_2, \dots, e_n]$, where e_j has 1 in the j th position and 0 everywhere else. The resulting orthogonal matrix $B^i = [\beta_1^i, \dots, \beta_n^i]$ contains the desired coefficients in its columns.

As an example, with $n = 2$, we have $\beta_1^i = [1, a^i]^T$ and the Gram-Schmidt orthogonalization process produces

$$\left[\begin{bmatrix} 1 \\ a^i \end{bmatrix}, \begin{bmatrix} 0 \\ 1 \end{bmatrix} \right] \rightarrow \left[\begin{bmatrix} 1 \\ a^i \end{bmatrix}, \begin{bmatrix} -a^i \\ 1 \end{bmatrix} \right] \quad (10)$$

so that $\beta_2^i = [-a^i, 1]^T$. This gives the coefficients in (2) and Fig. 1. With $n = 3$, we would have $\beta_1^i = [1, a_1^i, a_2^i]^T$ and the Gram-Schmidt orthogonalization process produces

$$\left[\begin{bmatrix} 1 \\ a_1^i \\ a_2^i \end{bmatrix}, \begin{bmatrix} 0 \\ 1 \\ 0 \end{bmatrix}, \begin{bmatrix} 0 \\ 0 \\ 1 \end{bmatrix} \right] \rightarrow \left[\begin{bmatrix} 1 \\ a_1^i \\ a_2^i \end{bmatrix}, \begin{bmatrix} -a_1^i \\ (a_2^i)^2 + 1 \\ -a_1^i a_2^i \end{bmatrix}, \begin{bmatrix} -a_2^i \\ 0 \\ 1 \end{bmatrix} \right] \quad (11)$$

so that $\beta_2^i = [-a_1^i, (a_2^i)^2 + 1, -a_1^i a_2^i]^T$ and $\beta_3^i = [-a_2^i, 0, 1]^T$. It should be clear how to modify the first-layer of the BumpNet module in Fig. 1 in the $n = 3$ case, and beyond.

It can be shown that the generalization of (4) to find the support size in the n -dimensional case is

$$l_j^i = \frac{s_j^i + \bar{s}_j^i}{\|\beta_j^i\|}, \quad j = 1, \dots, n, \quad (12)$$

where $\|\cdot\|$ denotes the Euclidean norm, while the generalization of (5) to obtain the bump center coordinates is

$$\begin{bmatrix} c_1^i \\ \vdots \\ c_n^i \end{bmatrix} = (B^i)^{-1} \begin{bmatrix} \bar{s}_1^i - s_1^i \\ \vdots \\ \bar{s}_n^i - s_n^i \end{bmatrix}. \quad (13)$$

2.3. Detailed Training Procedure

As can be seen in (12), in order to obtain a nonvanishing bump support, we must have $s_j^i + \bar{s}_j^i > 0$, for $j = 1, \dots, n$. To achieve this, rather than training the biases s_j^i and \bar{s}_j^i directly, we employ a reparametrization. First, we introduce trainable parameters $W_j^i \in R$ such that

$$l_j^i = \exp(W_j^i) > 0, \quad j = 1, \dots, n. \quad (14)$$

In addition, in order to keep the center coordinates (c_1^i, \dots, c_n^i) in (13) of each bump in or around the PDE domain, we introduce trainable parameters $v_j^i \in R$ such that

$$c_j^i = x_{jl} + \frac{1}{2}(\tanh(v_j^i) + 1)(x_{jr} - x_{jl}), \quad j = 1, \dots, n, \quad (15)$$

where $(x_{1l}, x_{1r}) \times \dots \times (x_{nl}, x_{nr})$ is the bounding box around Ω , with $x_{jl} < x_{jr}$, for $j = 1, \dots, n$. If the domain Ω is hyperrectangular, which is often the case, then (15) constrains the bumps to be inside the domain. This enables BumpNet to effectively model complicated functions, such as the solution of the Helmholtz PDE (as is shown in Section 3.1.1).

Once the parameters W_j^i and v_j^i are updated at each iteration of gradient descent, the values of l_j^i and c_j^i are com-

puted via (14) and (15), respectively, and the updated values of the biases s_j^i and \bar{s}_j^i can be obtained by solving the system of equations given by (12) and (13). This system can be solved quite easily to give:

$$\begin{aligned} s_j^i &= \frac{1}{2} l_j^i \|\beta_j^i\| - \frac{1}{2} \sum_{k=1}^n c_k^i \beta_k^i, \quad j = 1, \dots, n, \\ \bar{s}_j^i &= \frac{1}{2} l_j^i \|\beta_j^i\| + \frac{1}{2} \sum_{k=1}^n c_k^i \beta_k^i, \quad j = 1, \dots, n. \end{aligned} \quad (16)$$

The remaining weights in the neural network are trained as usual. The procedure for training a BumpNet for regression is summarized in Algorithm 1.

Algorithm 1 Training BumpNet for Regression.

Input: Training data $\{(\mathbf{x}_1, y_1), \dots, (\mathbf{x}_N, y_N)\}$;
Hyperparameters: Number of bumps m , learning rate η , number of iterations T ;
Trainable Parameters: $\theta = \{a_j^i, W_j^i, v_j^i, p^i, h^i\}$;
Initialization: Using Eqs. 14 and 15, initialize $\{a_j^i, W_j^i, v_j^i\}$ such that the bumps are uniformly distributed over the domain bounding box and parallel to its boundaries. Initialize $h_i = 1$ and $p_i = \log 3.5$ (all bumps have unit height with a sharp profile);
Training:
for $t = 1$ **to** T **do**
 for $i = 1$ **to** m **do**
 for $j = 1$ **to** n **do**
 Compute size l_j^i using (14);
 Compute center c_j^i using (15);
 Compute biases s_j^i and \bar{s}_j^i using (16);
 Compute loss $L(\theta) \leftarrow \frac{1}{N} \sum_{i=1}^N (\psi(\mathbf{x}_i) - y_i)^2$;
 Compute gradient $g \leftarrow \text{Grad}(L(\theta))$;
 Update trainable weights $\theta \leftarrow \text{Update}(\theta, g, \eta)$;

2.4. BumpNet Pruning during Training

Model reduction and h-adaptivity can be achieved by removing irrelevant bumps. A simple way to do it, which we adopt here, is to prune bumps for which the height parameter h_i falls below a certain pre-specified threshold hyperparameter $q > 0$. This is done dynamically, after each r training steps, where r is a hyperparameter. This dynamical pruning process can improve the convergence speed and accuracy of the resulting BumpNet.

2.5. Bump-PINNs

Consider a general PDE:

$$\begin{aligned} \mathcal{N}_{\mathbf{x}}[u(\mathbf{x})] &= f(\mathbf{x}), \quad \mathbf{x} \in \Omega, \\ \mathcal{B}_{\mathbf{x}}[u(\mathbf{x})] &= g(\mathbf{x}), \quad \mathbf{x} \in \partial\Omega, \end{aligned} \quad (17)$$

where \mathbf{x} may include space, time, and other physical variables, \mathcal{N} is a differential operator, \mathcal{B} is a boundary operator, u is the solution of rgw PDE, f is the source function, g is the boundary condition, and Ω is the domain of the PDE.

BumpNets can be trained to satisfy a PDE and approximate its solution, in the manner of physics-informed neural networks (PINN) (Raissi et al., 2019). The resulting algorithm is called Bump-PINN. Let $\hat{u}(\mathbf{x}; \mathbf{w})$ denote the neural network, where \mathbf{w} denotes the network weights. By applying Automatic Differentiation to calculate differential terms, the network is trained to minimize the loss function:

$$\begin{aligned} \mathcal{L}(\mathbf{w}) &= \frac{1}{N_r} \sum_{i=1}^{N_r} |\mathcal{N}_{\mathbf{x}}[\hat{u}(\mathbf{x}_i^r; \mathbf{w})] - f(\mathbf{x}_i^r)|^2 \\ &\quad + \frac{1}{N_b} \sum_{i=1}^{N_b} |\mathcal{B}_{\mathbf{x}}[\hat{u}(\mathbf{x}_i^b; \mathbf{w})] - g(\mathbf{x}_i^b)|^2 \end{aligned} \quad (18)$$

where where $\{\mathbf{x}_i^r\}_{i=1}^{N_r} \subset \Omega$ and $\{\mathbf{x}_i^b\}_{i=1}^{N_b} \subset \partial\Omega$ are residual and boundary points, respectively.

2.6. Bump-SAPINNs

Weighting schemes can be applied to the PINN loss function in order to improve convergence speed and accuracy. Here, we consider the Self-Adaptive PINN (SAPINN) weighting scheme of (McClenny & Braga-Neto, 2023), resulting in the Bump-SAPINN method (self-adaptive Bump-PINN). The original SAPINN requires full-batch training to update the self-adaptive weights, which can impose substantial memory and computational demands (although a modification to allow stochastic mini-batch training is also proposed in (McClenny & Braga-Neto, 2023)). In contrast, the proposed BumpNet architecture is highly efficient, with a parameter count that is 20 to 100 times smaller than that of standard multi-layer perceptrons (MLPs). Despite its compact design, BumpNet demonstrates comparable performance to SAPINN in leveraging self-adaptive weights, achieving similar accuracy in solution representation, as will be seen in Section 3. Moreover, BumpNet significantly reduces training time due to its lightweight architecture and efficient parameterization. These results highlight the advantages of BumpNet in terms of memory efficiency, computational speed, and scalability, making it a promising alternative to traditional PINN architectures for self-adaptive frameworks.

2.7. Bump-EDNN

To solve time-evolution PDEs, Bump-PINNs can be employed with bumps over the entire space-time domain. Here, we consider an alternative, namely, the recently-proposed evolutional deep neural networks (EDNN) (Du & Zaki, 2021). Consider a time-evolution PDE of the form

$$\begin{aligned} \frac{\partial u(\mathbf{x}, t)}{\partial t} &= \mathcal{N}_{\mathbf{x}}[u(\mathbf{x}, t)], \quad \mathbf{x} \in \Omega, t \in (0, T), \\ u(\mathbf{x}, 0) &= h(\mathbf{x}), \quad \mathbf{x} \in \Omega, \\ u(\mathbf{x}, t) &= g(\mathbf{x}, t), \quad \mathbf{x} \in \partial\Omega, t \in (0, T). \end{aligned} \quad (19)$$

A Bump-EDNN $\hat{u}(\mathbf{x}, \mathbf{w}(t))$ first determines an initial value for the weights $\mathbf{w}(t = 0)$ by fitting the initial condition $h(\mathbf{x})$ with a regular BumpNet, and then advances the solution by updating the weights $\mathbf{w}(t)$ using an estimate of the derivative $d\mathbf{w}(t)/dt$, while enforcing the lateral boundary conditions automatically using the method in (Lu et al., 2021b). Therefore, the Bump-EDNN approximates the solution with spatial bumps at each different times t , where the bumps change with $\mathbf{w}(t)$, but without further gradient descent training. To obtain the estimate of $d\mathbf{w}(t)/dt$, first note that replacing $\hat{u}(\mathbf{x}; \mathbf{w}(t))$ in the PDE, one obtains, by the chain rule of differentiation,

$$\frac{\partial \hat{u}(\mathbf{x}; \mathbf{w}(t))}{\partial t} = \frac{\partial \hat{u}(\mathbf{x}; \mathbf{w}(t))}{\partial \mathbf{w}(t)} \cdot \frac{d\mathbf{w}(t)}{dt} = \mathcal{N}_{\mathbf{x}}[\hat{u}(\mathbf{x}; \mathbf{w}(t))] \quad (20)$$

Hence, an approximation of the derivative at each time t can be obtained as

$$\frac{d\mathbf{w}(t)}{dt} \approx \arg \min_{\gamma \in \mathcal{W}} \sum_{i=1}^{N_w} \left(\frac{\partial \hat{u}(\mathbf{x}_i^w; \mathbf{w}(t))}{\partial \mathbf{w}(t)} \cdot \gamma - \mathcal{N}_{\mathbf{x}}[\hat{u}(\mathbf{x}_i^w; \mathbf{w}(t))] \right)^2, \quad (21)$$

where \mathcal{W} is the weight space, $\{\mathbf{x}_i^w\}_{i=1}^{N_w}$ is a specified set of collocation points covering the domain Ω , and all derivatives on the right-hand side can be computed by automatic differentiation. This minimization problem (21) can be solved using any standard optimization technique; here, we simply use the method proposed in (Du & Zaki, 2021), which is to solve the first-order optimal necessary conditions. Given the initial weight value $\mathbf{w}(t = 0)$ and $d\mathbf{w}(t)/dt$, the evolution of $\mathbf{w}(t)$ can be used any integration method, such as simple forward Euler method. Here, we use 3rd-order Runge-Kutta scheme for obtaining both good accuracy and computational speed.

The advantage of this approach for solving time-dependent PDEs is that the network only needs to be trained on the initial condition. Time propagation is handled by integration, eliminating the need for retraining at each time step. However, one still needs to solve the optimization problem

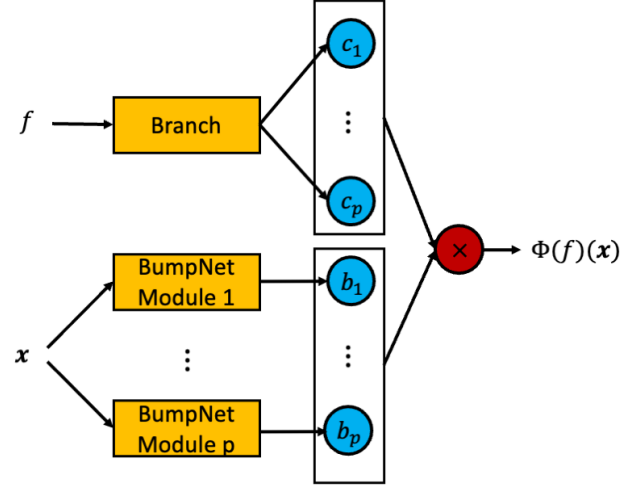


Figure 3: Network architecture of a Bump-DeepONet.

(21) at each new time step. To decrease the computational effort, only a subset of the weights $\mathbf{w}(t)$ of the BumpNet can be included in the computation of (21) and updated during time-stepping; here, only the height parameters h_i are updated. Thus, the bump shapes and locations are determined during training with the initial condition and kept fixed and subsequently only the coefficients that multiply each bump are updated. Another way to reduce the computational effort is to prune the smallest bumps after the BumpNet is trained on the initial condition, leading to a sparser basis expansion and smaller neural network. All of this mirrors the procedure used in classical basis-expansion methods for solving PDEs, such as proper orthogonal decomposition (POD) (Benner et al., 2015).

2.8. Bump-DeepONet

In a DeepONet (Lu et al., 2021a), the branch network takes a (suitably discretized) parameter f and encodes this information into a coefficient vector $c_1(f), \dots, c_p(f)$, while the trunk network takes the coordinate vector \mathbf{x} at which the solution is to be approximated, and computes basis vector outputs $b_1(\mathbf{x}), \dots, b_p(\mathbf{x})$. The output of the DeepONet is obtained by taking the dot product of these outputs:

$$\phi(f)(\mathbf{x}) = \sum_{i=1}^p c_i(f) \cdot b_i(\mathbf{x}). \quad (22)$$

(Sometimes a bias term is added, which can improve accuracy.) In Bump-DeepONet, the basis vector outputs $b_1(\mathbf{x}), \dots, b_p(\mathbf{x})$ are provided by BumpNet modules. These are trained in the usual manner along with the branch network. See Figure 3 for an illustration.

3. Results

In this section, we employ well-known PDE benchmarks to investigate the performance of Bump-PINN, Bump-EDNN, and Bump-DeepONet, comparing them to alternative methods in the literature.

3.1. Bump-PINN Performance

We evaluate the baseline Bump-PINN architecture against the baseline PINN (Raissi et al., 2019), self-adaptive PINN (McCleny & Braga-Neto, 2023), Bump-SAPINN (that is, a Bump-PINN with self-adaptive weights), as well as SPINN (Ramabathiran & Ramachandran), a method similar to BumpNets. Our evaluation considers accuracy (relative L1 error against the analytical solution), training time, and parameter count across a number of well-known PDE benchmarks. We use a exponential learning rate scheduler with scale 0.9 for every 1000 training steps.

3.1.1. INHOMOGENEOUS HELMHOLTZ EQUATION

$$u_{xx}(x, y) + u_{yy}(x, y) + k^2 u(x, y) = q(x, y), \quad (23)$$

where $(x, y) \in [-3, 3]^2$, $k = 1$, with zero boundary conditions. The forcing term $q(x, y)$ is manufactured to give the solution

$$u(x, y) = \sin(\pi x) \sin(\pi y). \quad (24)$$

The Bump-PINN is initialized with 10×10 bumps uniformly distributed over the domain (x, y) plane, and connected seamlessly. For training, a random batch of 10^4 collocation points within the domain $[-3, 3]^2$ and 200 uniformly distributed boundary points on each boundary are sampled. The network is trained using the Adam optimizer, with an initial learning rate of $7e-2$ for Bump-PINN and Bump-SAPINN and $1e-3$ for PINN and SAPINN.

Bump-PINN achieves an accurate prediction with only 280 parameters (Fig. 4). In contrast, PINN requires approximately 55 times more parameters to achieve high accuracy, that requires fewer parameters than deep neural network (Table 1). SPINN achieves similar accuracy and efficiency with 400 nodes.

3.1.2. TWO-DIMENSIONAL POISSON EQUATION

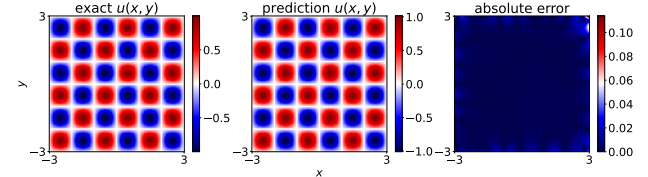
We now examine the application of Bump-PINN to the two-dimensional Poisson equation

$$\frac{\partial^2 u(x, y)}{\partial x^2} + \frac{\partial^2 u(x, y)}{\partial y^2} = 20\pi^2 \sin(2\pi x) \sin(4\pi y), \quad (25)$$

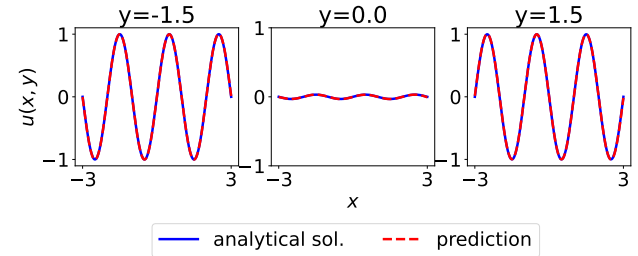
where $(x, y) \in D = [0, 1]^2$, $u(x, y) = 0$ for $x, y \in \partial D$ for zero boundary conditions. The solution is

$$u(x, y) = \sin(2\pi x) \sin(4\pi y) \quad (26)$$

For this problem, Bump-PINN is initialized with a structured grid of 6×6 bumps on the two-dimensional plane without gaps. The initial learning rate is 0.5. Bump-PINN achieves a mean squared error (MSE) of 9.61×10^{-4} on the test set, which is slightly less accurate than SPINN. However, Bump-PINN demonstrates remarkable computational efficiency, completing training in around 1 minute, which is 20x faster than SPINN (Fig. 5 and Table 1). Both Bump-PINN and SPINN achieve similar accuracy with fewer parameters than the baseline PINN counterpart.



(a) (Left) Exact solution. (Middle) Prediction of the BumpNet-PINN. (Right) Absolute difference.



(b) Comparison of prediction and exact solution on $y = -1.5, 0.0, 1.5$ over $x \in [-3, 3]$.

Figure 4: Helmholtz equation with BumpNet-PINN.

3.1.3. HEAT EQUATION

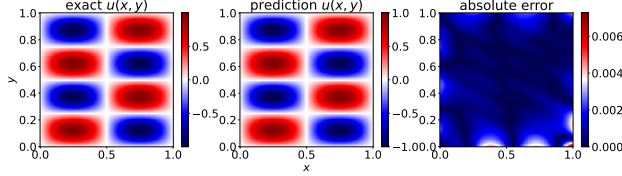
This benchmark evaluates Bump-PINN in a simple time-evolution problem, where BumpNet is trained on the spatial and temporal domains simultaneously, i.e., with “space-time” bumps. The benchmark is the 1D heat equation

$$\frac{\partial u(x, t)}{\partial t} = \alpha \frac{\partial^2 u(x, t)}{\partial x^2} + 2 \sin(\pi x), \quad (27)$$

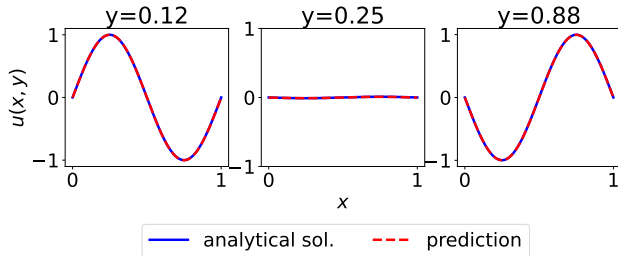
where $(x, t) \in [0, 1] \times [0, 5]$, with initial condition $u(x, 0) = \sin(2\pi x)$. The analytical solution to this equation is given by

$$u(x, t) = e^{-4\pi^2 \alpha t} \sin(2\pi x) + \frac{2}{\pi^2 \alpha} (1 - e^{-\pi^2 \alpha t}) \sin(\pi x), \quad (28)$$

where we set $\alpha = 1$.



(a) (Left) Exact solution. (Middle) Prediction of the BumpNet PINN. (Right) Absolute difference.



(b) Comparison of prediction and exact solution on $x, y \in [0, 1]^2$.

Figure 5: BumpNet-PINN for the Poisson equation.

We applied Bump-PINN with 20×6 structured bumps along the spatial and temporal dimensions, resulting in 840 parameters. We use higher resolution on the x-axis to capture the sinusoidal curve. The Bump-PINN was compared to a PINN based on a MLP with 15 layers of 15 nodes each, containing 3,421 parameters, and SPINN with 200 nodes and 1,021 parameters. Despite its smaller parameter count, Bump-PINN demonstrated superior predictive accuracy in capturing complex solution geometries (Fig. 6 and Table 1). This efficiency underscores its architectural advantages. Notably, SPINN faces convergence challenges for this problem and requires supplemental finite difference methods to achieve an accurate solution (Ramabathiran & Ramachandran). In contrast, BumpNet is flexible and can effectively represent intricate solution geometries without additional numerical methods.

3.1.4. ADVECTION EQUATION WITH PERIODIC BOUNDARY CONDITION

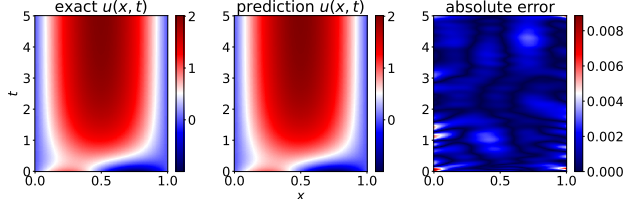
Another example of a space-time problem is the 1D advection equation

$$\frac{\partial u(x, t)}{\partial t} + \nu \frac{\partial u(x, t)}{\partial x} = 0, \quad (29)$$

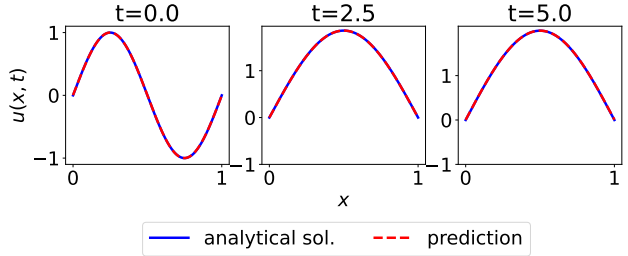
where $x \in [0, 2\pi]$, $t \in [0, 1]$ with initial condition $u(x, 0) = \sin(x)$ and periodic boundary condition $u(0, t) = u(2\pi, t)$. The solution is

$$u(x, t) = \sin(x - \nu t) \quad (30)$$

In this experiment, we set $\nu = 30$, a regime where PINN fails to train (McClenny & Braga-Neto, 2023; Braga-Neto,



(a) (Left) Exact solution. (Middle) Prediction of the Bump-PINN. (Right) Absolute difference.



(b) Comparison of prediction and exact solution on $t = [0, 5.0]$ and $x \in [0, 1]$.

Figure 6: Bump-PINN for the Heat equation.

2022). The bumps in BumpNet are initialized on a (2×11) grid for x-axis and t-axis. A self-adaptive loss function with a square mask is employed, where the self-adaptive weights are initialized to 1.0. Both BumpNet and the self-adaptive weights are optimized using the Adam optimizer with an initial learning rate of 0.02. Under these settings, the L1 error achieved is 2.3×10^{-3} . Furthermore, similar to PINN, Bump-PINN also fails to train when $\nu = 30$. This experiment highlights the efficiency of BumpNet compared to MLP within the self-adaptive framework.

3.2. Performance of Bump-PINN with Pruning

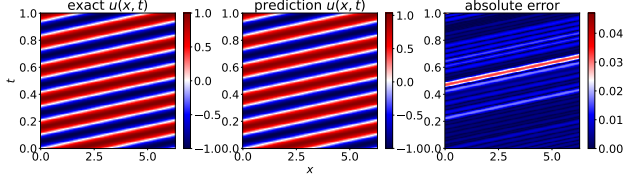
To investigate the possibility of performing automatic model order reduction with BumpNet (see Section 2.4), we compare the performance of Bump-PINN with and without pruning in the Helmholtz problem (Eq. (23)). Bumps with 0.15% lowest absolute amplitude are pruned for 4 times with each interval contained 2000 iterations. Since the pruned model has a different number of parameters, the optimizer is re-initialized for the pruned model, which introduces a spike in the training loss right after pruning, as seen in Fig. 8. Nevertheless, we can see in this figure that pruning accelerates training convergence over the baseline Bump-PINN without pruning. This suggests that removing non-essential bumps modifies the loss surface in a favorable way.

benchmark	method	L1 error	# param	train time (sec)
Advection Equation (60K epochs)	Bump-PINN	2.30e-03	154	28
	Bump-SAPINN	8.04e-03	154	113
	PINN	7.78e-02	83073	48
	SAPINN	3.07e-04	83073	727
	SPINN	6.33e-01	481	437
Heat Equation (20K epochs)	Bump-PINN	1.83e-03	840	12
	Bump-SAPINN	6.51e-03	840	111
	PINN	3.15e-02	3421	41
	SAPINN	4.56e-02	3421	144
	SPINN	2.18e+00	1021	291
Helmholtz Equation (70K epochs)	Bump-PINN	2.66e-02	1575	51
	Bump-SAPINN	7.92e-03	1575	406
	PINN	1.24e-01	83073	85
	SAPINN	5.04e-02	83073	1283
	SPINN	9.83e-01	1761	2265
Poisson Equation (100K epochs)	Bump-PINN	8.66e-04	252	61
	Bump-SAPINN	7.45e-03	252	79
	PINN	2.73e-02	83073	112
	SAPINN	2.78e-02	83073	1600
	SPINN	1.03e-04	481	1256

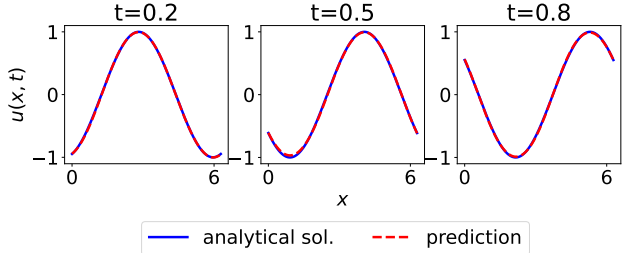
Table 1: Comparison of PINN, SAPINN, Bump-PINN, Bump-SAPINN, and SPINN.

benchmark	method	# collocation points	# boundary points
Helmholtz	PINN	1000	200
	SAPINN	10000	200
Poisson	PINN	1000	100
	SAPINN	10000	200
Heat	PINN	1000	200
	SAPINN	20000	1000
Advection	PINN	1000	200
	SAPINN	15000	1000

Table 2: Experimental Settings. “PINN” refers to the baseline PINN, Bump-PINN, and SPINN, while “SAPINN” refers to the baseline SAPINN and the Bump-SAPINN. The number of boundary points is per side.



(a) (Left) Exact solution. (Middle) Prediction of the Bump-PINN. (Right) Absolute difference.



(b) Comparison of precision and exact solution on $t = -1.5, 0.0, 1.5$ over $x \in [0, 6]$.

Figure 7: Bump-SAPINN for the linear advection equation.

3.3. Bump-EDNN Performance

In this section, we demonstrate the advantages of Bump-EDNN in comparison to the standard EDNN in solving time-dependent PDEs with significantly reduced computational cost and improved efficiency. We apply this approach on two-dimensional heat equation:

$$\begin{aligned} \frac{\partial u(x, y, t)}{\partial t} &= \nu \left(\frac{\partial^2 u(x, y, t)}{\partial x^2} + \frac{\partial^2 u(x, y, t)}{\partial y^2} \right), \\ (x, y) &\in [-\pi, \pi]^2 \\ u(x, y, 0) &= \sin(x) \sin(y) \\ u &= 0 \text{ on } \partial\Omega \end{aligned} \quad (31)$$

The analytical solution is

$$u(x, y, t) = \sin(x) \sin(y) \exp(-2\nu t), \quad (32)$$

where we set $\nu = 1$. We impose the boundary conditions on the neural networks using the approach in (Lu et al., 2021b). In the experiment, the parameter γ is solved for with tolerance $1e-4$. The EDNN is based on an MLP with four layers and 20 neurons per layer. The ODE system for evolving the weights is solved by the third-order Runge-Kutta solver, for a good balance between accuracy and computational time. We can see in Fig. 9 that Bump-EDNN is more accurate than EDNN, especially as time increases. We can see in Table 3 that Bump-EDNN converged faster than EDNN during training on the initial condition, and that the higher accuracy of Bump-EDNN is obtained with a much smaller number of parameters and faster solving time than EDNN. In particular, the time required for weight evolution, once the weights have been initialized by training

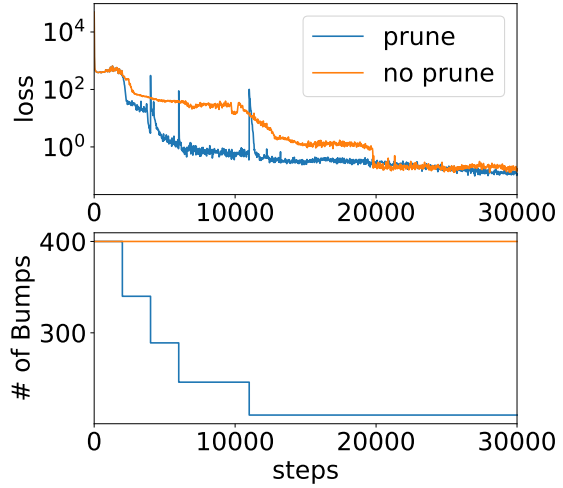


Figure 8: Training a Bump-Net with and without pruning.

	Bump-EDNN	EDNN
Architecture	6×6 bumps	4×20 MLP
# of trainable parameters	252	1341
# of evolving parameters	36	1341
Training time on initial condition	6m43s	8m24sec
L2 Error at $t = 1$	5e-4	1.4e-3
Time-evolution solving time	6sec	23m13sec

Table 3: Comparison of Bump-EDNN and EDNN.

on the initial condition, is almost three orders of magnitude shorter in the case of Bump-EDNN.

3.4. Bump-DeepONet Performance

To investigate Bump-DeepONet’s potential for operator learning, we consider a nonlinear diffusion-reaction PDE with a forcing term $f(x)$:

$$\frac{\partial u}{\partial t} = D \frac{\partial^2 u}{\partial x^2} + ku^2 + f(x), \quad (x, t) \in (0, 1] \times (0, 1], \quad (33)$$

where the reaction rate is $k = 0.01$ and the diffusion coefficient is $D = 0.01$. Zero initial and boundary conditions are used. The operator learning goal is to recover the map from the forcing term $f(x)$ to the corresponding solution $u(x, t)$. Following (Wang et al., 2021), the forcing function $f(x)$ is generated using a Gaussian Random Field (GRF) with a square exponential kernel, a length scale of 0.2, and a scale factor of 1.

For this task, we apply a 10×10 grid of bumps across the spatial and temporal domains. Bumps are constrained to be in the physical domain, as explained in Section 2.2.3, for efficient representation. We observed that Bump-DeepONet accurately solves the operator learning problem, as can be seen in Fig. 10 for a random test forcing function

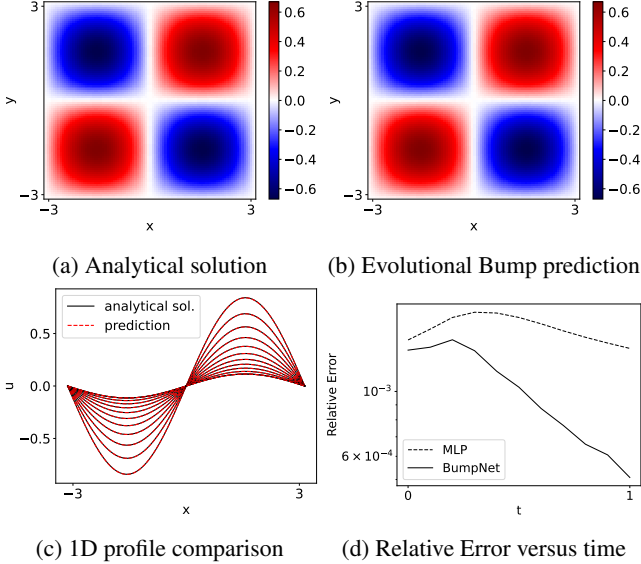


Figure 9: Bump-EDNN for the Heat equation. (a,b) Comparison between prediction and analytical solution at $t = 0.2$. (c) 1D profile comparison at $y = 1$. (b) Relative error of Bump-EDNN compared to EDNN.

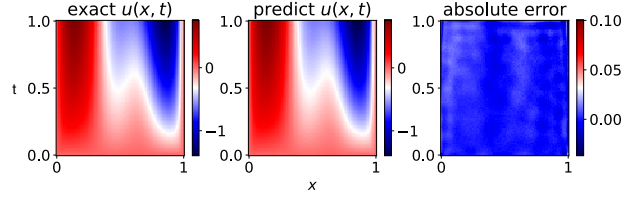
	Bump-DeepONet	DeepONet
Architecture of trunk	10×10	50 wide, 4 layers
Training time	86 sec (937.2 iter/sec)	158 sec (775.75 iter/sec)
# of param. in trunk	600	25600
Test Error	$8.12e-6$	$5.42e-6$

Table 4: Comparison of Bump-DeepONet with DeepONet.

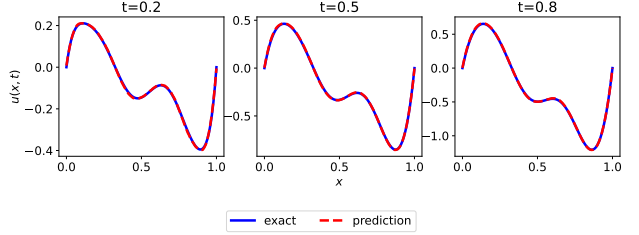
(not observed during training). Notably, Bump-DeepONet requires 100 times fewer parameters than the DeepONet while achieving comparable accuracy in this problem, as seen in Table 4. The trained Bump-DeepONet identifies the solution accurately by placing more bumps over complex regions (Fig. 10c). These results demonstrate that BumpNet enables efficient operator learning and serves as a highly parameter-efficient alternative to traditional MLP-based architectures.

4. Conclusion

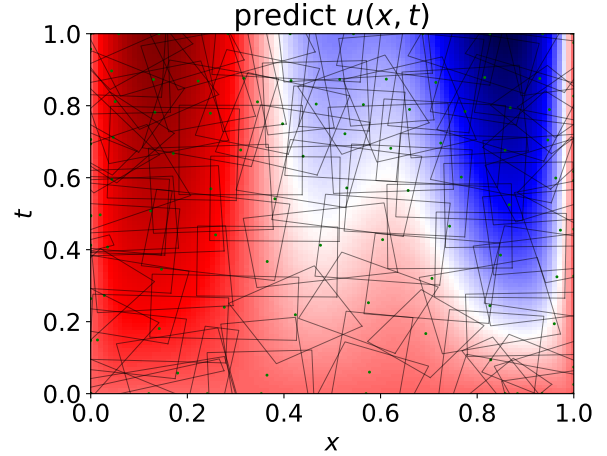
We introduced BumpNet, a parameter-efficient, fully-interpretable neural network architecture for learning PDE solutions. Extensive experiments demonstrated that BumpPINN, Bump-EDNN, and Bump-DeepONet obtain accurate solutions in physics-informed machine learning and operator learning problems, while requiring fewer parameters, shorter training time, and faster predictions than competing methods. A simple pruning technique based on the amplitudes of bumps achieves h-adaptivity while accelerating training convergence. In time-dependent partial differential equations (PDEs), BumpNets can be applied by



(a) Solution for a random test forcing function.



(b) Solution in (a) at different time slices.



(c) Bump locations and boundaries for the solution in (a).

Figure 10: Bump-DeepONet for a diffusion reaction PDE. In (c), dots and rectangles indicate bump centers and boundaries. More basis functions concentrate around areas of high gradients in the solution, achieving h-adaptivity.

using a Bump-PINN over the entire spatio-temporal domain, or by applying a Bump-EDNN, which only requires training a spatial BumpNet on the initial condition, and evolving its parameters using the evolutional neural network framework, which is fast while maintaining low error during time-stepping. Bump-DeepONet allows the application of BumpNets to operator learning by replacing the trunk network of a DeepONet with a BumpNet. This efficient parameterization reduces the size of the trunk by half and accelerates convergence when learning an operator. We believe that the efficiency and interpretability of the BumpNet architecture make it a promising new tool for advancing scientific machine learning and complex system modeling.

5. Funding

The work of STC and UBN was partially supported by the National Science Foundation under Grant Number 2225507, while IGK was partially supported by the US Department of Energy.

References

Bai, J., Liu, G.-R., Gupta, A., Alzubaidi, L., Feng, X.-Q., and Gu, Y. Physics-informed radial basis network (PIRBN): A local approximating neural network for solving nonlinear partial differential equations. *Computer Methods in Applied Mechanics and Engineering*, 415:116290, 2023. ISSN 00457825. doi: 10.1016/j.cma.2023.116290. URL <https://linkinghub.elsevier.com/retrieve/pii/S0045782523004140>.

Belytschko, T., Krongauz, Y., Organ, D., Fleming, M., and Krysl, P. Meshless methods: An overview and recent developments. *Computer Methods in Applied Mechanics and Engineering*, 139(1-4):3–47, December 1996. ISSN 00457825. doi: 10.1016/S0045-7825(96)01078-X. URL <https://linkinghub.elsevier.com/retrieve/pii/S004578259601078X>.

Benner, P., Gugercin, S., and Willcox, K. A survey of projection-based model reduction methods for parametric dynamical systems. *SIAM review*, 57(4):483–531, 2015.

Bollig, E. F., Flyer, N., and Erlebacher, G. Solution to PDEs using radial basis function finite-differences (RBF-FD) on multiple GPUs. *Journal of Computational Physics*, 231(21):7133–7151, August 2012. ISSN 00219991. doi: 10.1016/j.jcp.2012.06.030. URL <https://linkinghub.elsevier.com/retrieve/pii/S0021999112003452>.

Braga-Neto, U. Characteristics-Informed Neural Networks for Forward and Inverse Hyperbolic Problems, December 2022. URL <http://arxiv.org/abs/2212.14012>. arXiv:2212.14012 [physics].

Broomhead, D. S. Multivariable Functional Interpolation and Adaptive Networks. *Complex Systems*.

Cyr, E. C., Gulian, M. A., Patel, R. G., Perego, M., and Trask, N. A. Robust Training and Initialization of Deep Neural Networks: An Adaptive Basis Viewpoint. *Proceedings of Machine Learning Research*.

Du, Y. and Zaki, T. A. Evolutional deep neural network. *Physical Review E*, 104(4):045303, 2021.

Huang, G.-B., Zhu, Q.-Y., and Siew, C.-K. Extreme learning machine: Theory and applications. *Neurocomputing*, 70(1-3):489–501, December 2006. ISSN 09252312. doi: 10.1016/j.neucom.2005.12.126. URL <https://linkinghub.elsevier.com/retrieve/pii/S0925231206000385>.

Kansa, E. Multiquadratics—A scattered data approximation scheme with applications to computational fluid-dynamics—I surface approximations and partial derivative estimates. *Computers & Mathematics with Applications*, 19(8-9):127–145, a. ISSN 08981221. doi: 10.1016/0898-1221(90)90270-T. URL <https://linkinghub.elsevier.com/retrieve/pii/089812219090270T>.

Kansa, E. Multiquadratics—A scattered data approximation scheme with applications to computational fluid-dynamics—II solutions to parabolic, hyperbolic and elliptic partial differential equations. *Computers & Mathematics with Applications*, 19(8-9):147–161, b. ISSN 08981221. doi: 10.1016/0898-1221(90)90271-K. URL <https://linkinghub.elsevier.com/retrieve/pii/089812219090271K>.

Karniadakis, G. E., Kevrekidis, I. G., Lu, L., Perdikaris, P., Wang, S., and Yang, L. Physics-informed machine learning. *Nature Reviews Physics*, 3(6):422–440, 2021.

Lapedes, A. and Farber, R. *How Neural Nets Work*, pp. 331–346. WORLD SCIENTIFIC. ISBN 978-9971-5-0529-5 978-981-4434-10-2. doi: 10.1142/9789814434102_0012. URL https://www.worldscientific.com/doi/10.1142/9789814434102_0012.

Lu, L., Jin, P., and Karniadakis, G. E. DeepONet: Learning nonlinear operators for identifying differential equations based on the universal approximation theorem of operators. *Nature Machine Intelligence*, 3(3):218–229, March 2021a. ISSN 2522-5839. doi: 10.1038/s42256-021-00302-5. URL <http://arxiv.org/abs/1910.03193>. arXiv:1910.03193 [cs, stat].

Lu, L., Pestourie, R., Yao, W., Wang, Z., Verdugo, F., and Johnson, S. G. Physics-informed neural networks with hard constraints for inverse design. *SIAM Journal on Scientific Computing*, 43(6):B1105–B1132, 2021b.

McClenny, L. D. and Braga-Neto, U. M. Self-adaptive physics-informed neural networks. *Journal of Computational Physics*, 474:111722, 2023.

Montazer, G. A., Giveki, D., Karami, M., and Rastegar, H. Radial basis function neural networks: A review. *Comput. Rev. J.*, 1(1):52–74, 2018.

Raissi, M., Perdikaris, P., and Karniadakis, G. E. Physics-informed neural networks: A deep learning framework for solving forward and inverse problems involving nonlinear partial differential equations. *Journal of Computational Physics*, 378:686–707, 2019. ISSN 0021-9991. doi: 10.1016/j.jcp.2018.10.045. URL <https://www.sciencedirect.com/science/article/pii/S0021999118307125>.

Ramabathiran, A. A. and Ramachandran, P. SPINN: Sparse, Physics-based, and partially Interpretable Neural Networks for PDEs. *Journal of Computational Physics*, 445:110600. ISSN 00219991. doi: 10.1016/j.jcp.2021.110600. URL <http://arxiv.org/abs/2102.13037>.

Wang, L. Radial basis functions methods for boundary value problems: Performance comparison. *Engineering Analysis with Boundary Elements*, 84:191–205. ISSN 09557997. doi: 10.1016/j.enganabound.2017.08.019. URL <https://linkinghub.elsevier.com/retrieve/pii/S0955799717302539>.

Wang, S., Wang, H., and Perdikaris, P. Learning the solution operator of parametric partial differential equations with physics-informed DeepONets. *Science Advances*, 7(40):eabi8605, 2021. doi: 10.1126/sciadv.abi8605.

Zhang, L., Cheng, L., Li, H., Gao, J., Yu, C., Domel, R., Yang, Y., Tang, S., and Liu, W. K. Hierarchical deep-learning neural networks: finite elements and beyond. *Computational Mechanics*, 67:207–230, 2021.

Zhang, X., Song, K. Z., Lu, M. W., and Liu, X. Meshless methods based on collocation with radial basis functions. *Computational Mechanics*, 26(4):333–343. ISSN 0178-7675, 1432-0924. doi: 10.1007/s004660000181. URL <http://link.springer.com/10.1007/s004660000181>.